Geosci. Model Dev. Discuss., 7, 7937–7987, 2014
www.geosci-model-dev-discuss.net/7/7937/2014/
doi:10.5194/gmdd-7-7937-2014

Geoscientific Model Development Discussions
Open Access

A size-composition resolved aerosol model for simulating the dynamics of externally mixed particles: SCRAM (v 1.0)

S. Zhu, K. N. Sartelet, and C. Seigneur

CEREA, joint laboratory Ecole des Ponts ParisTech – EDF R&D, Université Paris-Est, 77455 Champs-sur-Marne, France

Received: 17 October 2014 – Accepted: 31 October 2014 – Published: 20 November 2014

Correspondence to: S. Zhu (zhus@cerea.enpc.fr)

Published by Copernicus Publications on behalf of the European Geosciences Union.

Abstract

A Size-Composition Resolved Aerosol Model (SCRAM) for simulating the dynamics of externally-mixed atmospheric particles is presented. This new model classifies aerosols by both composition and size, based on a comprehensive combination of all chemical species and their mass-fraction sections. All three main processes involved in aerosol dynamics (coagulation, condensation/evaporation and nucleation) are included. The model is first validated by comparison with a reference solution and with results of simulations using internally-mixed particles. The importance of representing the mixing state when modelling atmospheric aerosol concentrations is investigated in a box model simulation using data representative of air pollution in Greater Paris.

1 Introduction

Increasing attention is being paid to atmospheric particulate matter (PM), which is a major contributor to air pollution issues ranging from adverse health effects to visibility impairment (EPA, 2009; Pascal et al., 2013). Concentrations of $PM_{2.5}$ and PM_{10} are regulated in many countries, especially in North America and Europe. For example, regulatory concentration thresholds of 12 and 20 $\mu g\,m^{-3}$ have been set for $PM_{2.5}$ annual mass concentrations in the United States and Europe, respectively. Furthermore, particles influence the Earth's energy balance and global climate change (Myhre et al., 2013).

Three-dimensional Chemical-transport models (CTM) are often used to study and forecast the formation and distribution of PM. The size distribution of particles is often discretised into sections (e.g., Gelbard and Seinfeld, 1980; Zhang et al., 2004; Sartelet et al., 2007) or approximated by log-normal modes (e.g., Whitby and McMurry, 1997; Binkowski and Roselle, 2003). Moreover, CTM usually assume that particles are internally-mixed, i.e. each size section or log-normal mode has the same chemical composition, which may vary in space and time.

GMDD
7, 7937–7987, 2014

The internal-mixing assumption implies that particles of a same diameter (or in the same size section or log-normal mode) but originating from different sources have undergone sufficient mixing to achieve a common chemical composition for a given model grid cell and time. Although this assumption may be realistic far from emission sources, it may not be valid close to emission sources where the composition of new emitted particles can be very different from either background particles or particles from other sources. Usually, internally- and externally-mixed particles are not differentiated in most measurements, which may be size-resolved (e.g., cascade impactors) but not particle specific (McMurry, 2000). The use of mass spectrometers for individual particle analysis has shed valuable information on the chemical composition of individual particles. Consequently, there is a growing body of observations indicating that particles are mostly externally mixed (e.g., Hughes et al., 2000; Mallet et al., 2004; Healy et al., 2012; Deboudt et al., 2010).

The mixing state assumption may strongly influence aerosol chemistry and hygroscopic characteristics, influencing in turn particle diameters, optical properties, and radiative forcing (Lesins et al., 2002; Jacobson, 2001), and the number of particles that may become cloud condensation nuclei (CCN), because the activation of particles depends on their size and composition (Leck and Svensson, 2014). The mixing state may also influence the formation of secondary organic aerosols (SOA), by influencing the hydrophilic and/or organic absorbing properties of particles.

Although CTM usually assume that particles are internally-mixed, several models have been developed during the last sesquidecade to represent the external mixture of particles. A source-oriented model was developed by Kleeman et al. (1997) and Kleeman and Cass (2001) for regional modelling. In these models, each source is associated with a specific aerosol population, which may evolve in terms of size distribution and chemical composition, but does not mix with the other sources (i.c., particle coagulation is neglected). Riemer et al. (2009) modelled externally-mixed particles using a stochastic approach. However, such an approach is computationally expensive when the number of particles is high. To represent externally-mixed particles independently

GMDD
7, 7937–7987, 2014

of their sources and number concentrations, Jacobson et al. (1994) and Lu and Bowman (2010) considered particles that can be either internally- or externally-mixed (i.e., composed of a pure chemical species). Lu and Bowman (2010) used a threshold mass fraction to define whether the species is of significant concentration. Jacobson (2002) expanded on Jacobson et al. (1994) by allowing particles to have different mass fractions. Similarly, Oshima et al. (2009) discretised the fraction of black carbon in the total particle mass into sections of different chemical composition. Dergaoui et al. (2013) further expanded on these modelling approaches by discretising the mass fraction of any chemical species into sections, as well as the size distribution. For each size section, the mass fraction of each species is discretised into sections $F^+_{h-} = [F^-_h, F^+_h]$ (h varies from 1 to the number of mass fraction sections n_f with $F^-_1 = 0$, $F^-_{n_f} = 1$ and $F^-_h = F^+_{h-1}$), leading to a variety of possible particle compositions. Assuming that it is possible to have up to c chemical species in particles, let us denote f_i the mass fraction of species X_i ($1 \leq i \leq c$). Each particle is associated with a mass fraction vector $\boldsymbol{f} = (f_1, f_2, \cdots, f_{(c-1)})$, which defines the particle composition/$\boldsymbol{P}_g = (F^+_{g_1-}, F^+_{g_2-}, \cdots, F^+_{g_{(c-1)}-})$ with $f_i \in F^+_{g_i-}$. For a particle composition to be valid, $\sum_{i=1}^{(c-1)} F^-_{g_i} \leqslant 1$ must be satisfied. Note that f_c is not specified because it is constrained by mass conservation ($f_c = 1 - \sum_{i=1}^{(c-1)} f_i$). Based on this discretisation, Dergaoui et al. (2013) derived the equation for coagulation and validated their model by comparing the results obtained for internal and external mixing, as well as by comparing both approaches against an exact solution. However, processes such as condensation/evaporation and nucleation were not modelled.

This work presents a new Size-composition Resolved Aerosol Model (SCRAM), which expends on the model of Dergaoui et al. (2013) by including condensation/evaporation and nucleation processes. Section 2 describes the model. Equations for the dynamic evolution of particles by condensation/evaporation are derived. A thermodynamic equilibrium method may be used in SCRAM to compute the evolution of the particle chemical composition by condensation/evaporation. Redistribution algorithms,

GMDD
7, 7937–7987, 2014

which allow section bounds not to vary, are also presented for future 3-D applications. Model validation is presented in Sect. 3 by comparing the changes in the particle size distribution due to condensational growth for both externally- and internally-mixed particles. Section 4 presents an application of the model with realistic concentrations over Greater Paris.

2 Model description

This section presents the aerosol general dynamic equations and the structure of the model. First, the formulation of the dynamic evolution of the aerosol size distribution and chemical composition by condensation-evaporation is introduced. Since it is necessary in 3-D CTM to maintain fixed size and composition section bounds, we present algorithms to redistribute particle mass and number according to fixed section bounds. For computational efficiency, a bulk equilibrium method, which assumes an instantaneous equilibrium between the gas and particle phases, is introduced. Finally, the overall structure of the model is described. In particular, the treatment of the different mixing processes to ensure the numerical stability of the model is discussed.

Particle dynamics is mostly governed by three processes: coagulation, condensation/evaporation, and nucleation. Nucleation refers to the formation of ultra fine particles from gaseous molecules. SCRAM uses the parametrisation of Vehkamäki et al. (2002) for the homogeneous binary nucleation of sulphate and water. It was adopted from the existing SIREAM code (Debry et al., 2007). It may be replaced by a better parametrisation in future versions, because it may lead to unrealistic results under some extreme conditions (Zhang et al., 2010). For coagulation, SCRAM uses the code of Dergaoui et al. (2013) to simulate the collisions of particles caused by Brownian motion. Condensation/evaporation describe the mass transfer process between the gas and the particle phases. It is essential to include condensation/evaporation, because this process not only largely influences the size distribution of aerosols, but may also change the composition of particles significantly.

GMDD
7, 7937–7987, 2014

2.1 Condensation–evaporation algorithm

The focus of the following subsections is the formulation and implementation of the condensation/evaporation process. Equations are derived to describe the change with time of the mass concentrations of chemical species in terms of particle compositions.

2.1.1 Dynamic equation for condensation/evaporation

Let us denote m_i the mass concentration of species X_i ($1 \le i \le c$) in a particle and $\boldsymbol{x}$ the vector representing the mass composition of the particle $\boldsymbol{x} = (m_1, m_2, \cdots, m_c)$. Following Riemer et al. (2009), the change with time of the number concentration $n(\boldsymbol{x}, t)$ ($\mathrm{m}^{-3}\,\mu\mathrm{g}^{-1}$) of multi-species particles by condensation/evaporation can be represented by the following equation:

$$\frac{\partial n}{\partial t} = -\sum_{i=1}^{c} \frac{\partial (I_i n)}{\partial m_i} \tag{1}$$

where I_i ($\mu\mathrm{g\,s}^{-1}$) is the mass transfer rate between the gas and particle phases for species X_i. It may be written as follows:

$$I_i = \frac{\partial m_i}{\partial t} = 2\pi\, D_i^{\mathrm{g}}\, d_{\mathrm{p}}\, f(Kn, \alpha_i) \left(c_i^{\mathrm{g}}(t) - K_{\mathrm{e}}(d_{\mathrm{p}})\, c_i^{\mathrm{eq}}(\boldsymbol{x}, t) \right) \tag{2}$$

where D_i^{g} is the molecular diffusivity of condensing/evaporating species in the air, and d_{p} and c_i^{g} are the particle wet diameter and the gas phase concentration of species X_i, respectively. Non-continuous effects are described by $f(Kn, \alpha_i)$ (Dahneke, 1983) which depends on the Knudsen number, $Kn = \frac{2\lambda}{d_{\mathrm{p}}}$ (with λ the air mean free path), and on the accommodation coefficient α_i:

$$f(Kn, \alpha_i) = \frac{1 + Kn}{1 + 2Kn(1 + Kn)/\alpha_i} \tag{3}$$

GMDD
7, 7937–7987, 2014

$K_e(d_p)$ represents the Kelvin effect (for ultra fine particles, the curvature tends to inhibit condensation):

$$K_e(d_p) = \exp\left(\frac{4\,\sigma\,v_p}{R\,T\,d_p}\right) \tag{4}$$

with R the ideal gas constant, σ the particle surface tension and v_p the particle molar volume. The local equilibrium gas concentration c_i^{eq} is computed using the reverse mode of the thermodynamic model ISORROPIA (Nenes et al., 1998) for inorganic compounds. In the current version of SCRAM, organic compounds are assumed to be at thermodynamic equilibrium with the gas phase and condensation/evaporation is computed as described in Sect. 2.2.

2.1.2 Dynamic equation as a function of mass fractions

Following the composition discretisation method of Dergaoui et al. (2013), each particle is represented by a vector $\boldsymbol{p} = (\boldsymbol{f}, m)$, which contains the mass fraction vector $\boldsymbol{f} = (f_1, f_2, \cdots, f_{(c-1)})$ of the first $(c-1)$ species and the total mass $m = \sum_{i=1}^{c} m_i$.

In Eq. (1), the chemical composition of particles is described by the vector $\boldsymbol{x}$ which contains the mass concentration of each species. After the change of variable through a $[c \times c]$ Jacobian matrix from $n(\boldsymbol{x}, t)$ to $\overline{n}(\boldsymbol{p}, t)$ (see Appendix A for detail), Eq. (1) becomes:

$$\frac{\partial \overline{n}}{\partial t} = -\sum_{i=1}^{(c-1)} \frac{\partial\left(H_i \overline{n}\right)}{\partial f_i} - \frac{\partial\left(I_0 \overline{n}\right)}{\partial m} \tag{5}$$

with $I_0 = \sum_{i=1}^{c} I_i$, $H_i = \frac{\partial f_i}{\partial t}$. As $f_i = \frac{m_i}{m}$ is the mass fraction of species X_i, we may write:

$$H_i = \frac{1}{m}\frac{\partial m_i}{\partial t} - \frac{m_i}{m^2}\frac{\partial m}{\partial t} = \frac{I_i - f_i I_0}{m} \tag{6}$$

GMDD
7, 7937–7987, 2014

The change with time of $q_i = n\ m_i$, the mass concentration of species X_i, can be expressed as follows:

$$\frac{\partial q_i}{\partial t} = \frac{\partial n}{\partial t} m_i + \frac{\partial m_i}{\partial t} n \tag{7}$$

After the change of variables from $q_i(\boldsymbol{x}, t)$ to $\overline{q_i}(\boldsymbol{p}, t)$ (see Appendix A), Eq. (7) becomes:

$$\frac{\partial \overline{q_i}}{\partial t} = -m\ f_i \frac{\partial \overline{n}}{\partial t} + \overline{n}\ I_i \tag{8}$$

2.1.3 Discretisation

As SCRAM is a size-composition resolved model, both particle size and composition are discretised into sections. The particle mass distribution $Q[m_{\min}, m_{\max}]$ is first divided into N_b size sections $[m_k^-, m_k^+]$ ($k = 1, \ldots, N_b$ and $m_{k-1}^+ = m_k^-$), defined by discretising particle diameters $[d_{\min}, d_{\max}]$ with $d_{\min}$ and $d_{\max}$, the lower and upper particle diameters, respectively, and $m_k = \frac{\pi\ \rho\ d_k^3}{6}$. For each of the first $(c-1)$ species, the mass fraction is discretised into N_f fraction ranges. The hth fraction range is represented by the range $F_{h\_}^+ = [f_h^-, f_h^+]$ where $f_{h-1}^+ = f_h^-$, $f_{\min} = 0$ and $f_{\max} = 1$. Within each size section k, particles are categorised into N_p composition sections, which are defined by the valid combinations of the fraction ranges of the $(c-1)$ species. The gth composition section can be represented by $\boldsymbol{P}_g = (F_{g1\_}^+, F_{g2\_}^+, \cdots, F_{gc-1\_}^+)$. Given the mass fraction discretisation, those composition sections are automatically generated by an iteration on all possible combinations $({N_f}^{(c-1)})$ of the $(c-1)$ species and N_f fraction ranges. Only the composition sections that satisfy $\sum_{i=1}^{(c-1)} {F_{gi}}^- \leqslant 1$ are kept.

The particle mass distribution is discretised into $(N_b \times N_p)$ sections. Each section j ($j = 1, \ldots, N_b \times N_c$) corresponds to a size section k ($k = 1, \ldots, N_b$) and to a composition section $g = (g_1, \ldots, g_{(c-1)})$ with $g = 1, \ldots, N_p$, $g_h = 1, \ldots, N_f$ with $h = 1, \ldots, (c-1)$. The

GMDD
7, 7937–7987, 2014

total concentration Q_i^j of species i in the jth section can be calculated as follows:

$$Q_i^j = \int_{m_k^-}^{m_k^+} \int_{f_{g_1}^-}^{f_{g_1}^+} \cdots \int_{f_{g_{(c-1)}}^-}^{f_{g_{(c-1)}}^+} \overline{q_i}(m, f_{g_1}, \ldots, f_{g_{(c-1)}}) \mathrm{d}m \mathrm{d}f_{g_1} \ldots \mathrm{d}f_{g_{(c-1)}} \tag{9}$$

Similarly, the number concentration N^j of the jth section may be written as follows:

$$N^j = \int_{m_k^-}^{m_k^+} \int_{f_{g_1}^-}^{f_{g_1}^+} \cdots \int_{f_{g_{(c-1)}}^-}^{f_{g_{(c-1)}}^+} \overline{n}(m, f_{g_1}, \ldots, f_{g_{(c-1)}}) \mathrm{d}m \mathrm{d}f_{g_1} \ldots \mathrm{d}f_{g_{(c-1)}} \tag{10}$$

The time derivation of Eq. (10) leads to:

$$\frac{\partial N^j}{\partial t} = \overbrace{\int_{m_k^-}^{m_k^+} \int_{f_{g_1}^-}^{f_{g_1}^+} \cdots \int_{f_{g_{(c-1)}}^-}^{f_{g_{(c-1)}}^+} \frac{\partial \overline{n}}{\partial t} \mathrm{d}m \mathrm{d}f_{g_1}, \ldots, \mathrm{d}f_{g_{(c-1)}}}^{A} + \overbrace{\frac{\mathrm{d}m_k^+}{\mathrm{d}t} \int_{f_{g_1}^-}^{f_{g_1}^+} \cdots \int_{f_{g_{(c-1)}}^-}^{f_{g_{(c-1)}}^+} \overline{n}\left(m_k^+, f_{g_1}, \ldots, f_{g_{(c-1)}}\right) \mathrm{d}f_{g_1}, \ldots, \mathrm{d}f_{g_{(c-1)}} - \frac{\mathrm{d}m_k^-}{\mathrm{d}t} \int_{f_{g_1}^-}^{f_{g_1}^+} \cdots}^{B} \tag{11}$$

GMDD
7, 7937–7987, 2014

$$\overbrace{\int_{f^-_{g_{(c-1)}}}^{f^+_{g_{(c-1)}}} \overline{n}\left(m_k^-, f_{g_1}, \ldots, f_{g_{(c-1)}}\right) \mathrm{d}f_{g_1}, \ldots, \mathrm{d}f_{g_{(c-1)}}}^{B}$$

$$+ \sum_{i=1}^{(c-1)} \left[\frac{\mathrm{d}f^+_{g_i}}{\mathrm{d}t} \int_{m_k^-}^{m_k^+} \int_{f^-_{g_1}}^{f^+_{g_1}} \cdots \int_{f^-_{g_{i-1}}}^{f^+_{g_{i-1}}} \int_{f^-_{g_{i+1}}}^{f^+_{g_{i+1}}} \cdots \int_{f^-_{g_{(c-1)}}}^{f^+_{g_{(c-1)}}} \overline{n}\left(m, f_{g_1}, \ldots, f_{g_{i-1}}, f^+_{g_i}, f_{g_{i+1}}, \ldots, f_{g_{(c-1)}}\right) \right.$$

$$\mathrm{d}m\mathrm{d}f_{g_1} \ldots \mathrm{d}f_{g_{i-1}} \mathrm{d}f_{g_{i+1}} \ldots \mathrm{d}f_{g_{(c-1)}} - \frac{\mathrm{d}f^-_{g_i}}{\mathrm{d}t} \int_{m_k^-}^{m_k^+} \int_{f^-_{g_1}}^{f^+_{g_1}} \cdots \int_{f^-_{g_{i-1}}}^{f^+_{g_{i-1}}} \int_{f^-_{g_{i+1}}}^{f^+_{g_{i+1}}} \cdots$$

$$\left. \int_{f^-_{g_{(c-1)}}}^{f^+_{g_{(c-1)}}} \overline{n}\left(m, f_{g_1}, \ldots, f_{g_{i-1}}, f^-_{g_i}, f_{g_{i+1}}, \ldots, f_{g_{(c-1)}}\right) \mathrm{d}m\mathrm{d}f_{g_1} \ldots \mathrm{d}f_{g_{i-1}} \mathrm{d}f_{g_{i+1}} \ldots \mathrm{d}f_{g_{(c-1)}} \right]$$

Replacing $\frac{\partial \overline{n}}{\partial t}(m, f_{g_1}, \ldots, f_{g_{(c-1)}})$ by Eq. (5), we have

$$A = \int_{m_k^-}^{m_k^+} \int_{f^-_{g_1}}^{f^+_{g_1}} \cdots \int_{f^-_{g_{(c-1)}}}^{f^+_{g_{(c-1)}}} \left[-\frac{\partial(I_0 n)}{\partial m} - \sum_{x=1}^{(c-1)} \frac{\partial(H_{g_x} n)}{\partial f_{g_x}} \right] \mathrm{d}m\mathrm{d}f_{g_1} \ldots \mathrm{d}f_{g_{(c-1)}} \quad (12)$$

GMDD
7, 7937–7987, 2014

and using $I_0 = \frac{\mathrm{d}m}{\mathrm{d}t}$, $H_{g_i} = \frac{\mathrm{d}f_{g_i}}{\mathrm{d}t}$ and $\frac{\partial f_{g_i}}{\partial f_{g_l}} = 0$ when $i \neq l$

$$A = -\left\{ \frac{\mathrm{d}m_k^+}{\mathrm{d}t} \int_{f_{g_1}^-}^{f_{g_1}^+} \cdots \int_{f_{g_{(c-1)}}^-}^{f_{g_{(c-1)}}^+} \overline{n}(m_k^+, f_{g_1}, \ldots, f_{g_{(c-1)}}) \mathrm{d}m \mathrm{d}f_{g_1} \ldots \mathrm{d}f_{g_{(c-1)}} - \frac{\mathrm{d}m_k^-}{\mathrm{d}t} \int_{f_{g_1}^-}^{f_{g_1}^+} \cdots \right. \tag{13}$$

$$\int_{f_{g_{(c-1)}}^-}^{f_{g_{(c-1)}}^+} \overline{n}(m_k^-, f_{g_1}, \ldots, f_{g_{(c-1)}}) \mathrm{d}m \mathrm{d}f_{g_1} \ldots \mathrm{d}f_{g_{(c-1)}} + \sum_{i=1}^{(c-1)} \left[\frac{\mathrm{d}f_{g_i}^+}{\mathrm{d}t} \int_{m_k^-}^{m_k^+} \int_{f_{g_1}^-}^{f_{g_1}^+} \cdots \int_{f_{g_{i-1}}^-}^{f_{g_{i-1}}^+} \int_{f_{g_{i+1}}^-}^{f_{g_{i+1}}^+} \cdots \right.$$

$$\left. \int_{f_{g_{(c-1)}}^-}^{f_{g_{(c-1)}}^+} \overline{n}(m, f_{g_1}, \ldots, f_{g_{i-1}}, f_{g_i^+}, f_{g_{i+1}}, \ldots, f_{g_{(c-1)}}) \mathrm{d}m \mathrm{d}f_{g_1} \ldots \mathrm{d}f_{g_{i-1}} \mathrm{d}f_{g_{i+1}} \ldots \mathrm{d}f_{g_{(c-1)}} \right.$$

$$\left. - \frac{\mathrm{d}f_{g_i}^-}{\mathrm{d}t} \int_{m_k^-}^{m_k^+} \int_{f_{g_1}^-}^{f_{g_1}^+} \cdots \int_{f_{g_{i-1}}^-}^{f_{g_{i-1}}^+} \int_{f_{g_{i+1}}^-}^{f_{g_{i+1}}^+} \cdots \int_{f_{g_{(c-1)}}^-}^{f_{g_{(c-1)}}^+} \overline{n}(m, f_{g_1}, \ldots, f_{g_{i-1}}, f_{g_i^-}, f_{g_{i+1}}, \ldots, f_{g_{(c-1)}}) \right.$$

$$\left. \mathrm{d}m \mathrm{d}f_{g_1} \ldots \mathrm{d}f_{g_{i-1}} \mathrm{d}f_{g_{i+1}} \ldots \mathrm{d}f_{g_{(c-1)}} \right] \Bigg\}$$

So $A = -B$, thus

$$\frac{\partial N^j}{\partial t} = (A + B) = 0 \tag{14}$$

which is expected since condensation/evaporation does not affect the total number of particles.

GMDD
7, 7937–7987, 2014

Similarly, an equation of change can be derived for Q_i^j. In order to simplify the writing of the equations, the following abbreviations are introduced:

$$f_{g_1^{(c-1)}} = f_{g_1}, \ldots, f_{g_{(c-1)}}$$

$$f_{g_1^{(c-1)} \setminus i} = f_{g_1}, \ldots, f_{g_{i-1}}, f_{g_{i+1}}, \ldots, f_{g_{(c-1)}}$$

$$\mathrm{d}f_{g_1^{(c-1)}} = \mathrm{d}f_{g_1} \ldots \mathrm{d}f_{g_{(c-1)}}$$

$$\mathrm{d}f_{g_1^{(c-1)} \setminus i} = \mathrm{d}f_{g_1} \ldots \mathrm{d}f_{g_{i-1}} \mathrm{d}f_{g_{i+1}} \ldots \mathrm{d}f_{g_{(c-1)}}$$

$$\int_{f^-_{g_1^{(c-1)}}}^{f^+_{g_1^{(c-1)}}} = \int_{f^-_{g_1}}^{f^+_{g_1}} \ldots \int_{f^-_{g_{(c-1)}}}^{f^+_{g_{(c-1)}}}$$

$$\int_{f^-_{g_1^{(c-1)} \setminus i}}^{f^+_{g_1^{(c-1)} \setminus i}} = \int_{f^-_{g_1}}^{f^+_{g_1}} \ldots \int_{f^-_{g_{i-1}}}^{f^+_{g_{i-1}}} \int_{f^-_{g_{i+1}}}^{f^+_{g_{i+1}}} \ldots \int_{f^-_{g_{(c-1)}}}^{f^+_{g_{(c-1)}}}$$

GMDD
7, 7937–7987, 2014

The time derivation of Eq. (9) leads to:

$$\frac{\partial Q_i^j}{\partial t} = \int_{m_k^-}^{m_k^+} \int_{f_{g_1^{(c-1)}}^-}^{f_{g_1^{(c-1)}}^+} \frac{\partial \overline{q_i}}{\partial t} \mathrm{d}m\mathrm{d}f_{g_1^{(c-1)}}$$

$$+ \frac{\mathrm{d}m_k^+}{\mathrm{d}t} \int_{f_{g_1^{(c-1)}}^-}^{f_{g_1^{(c-1)}}^+} \overline{q_i}(m_k^+, f_{g_1^{(c-1)}}) \mathrm{d}f_{g_1^{(c-1)}} - \frac{\mathrm{d}m_k^-}{\mathrm{d}t} \int_{f_{g_1^{(c-1)}}^-}^{f_{g_1^{(c-1)}}^+} \overline{q_i}(m_k^-, f_{g_1^{(c-1)}}) \mathrm{d}f_{g_1^{(c-1)}}$$

$$+ \sum_{i=1}^{(c-1)} \left[\frac{\mathrm{d}f_{g_1^{(c-1)}}^+}{\mathrm{d}t} \int_{m_k^-}^{m_k^+} \int_{f_{g_1^{(c-1)}\setminus i}^-}^{f_{g_1^{(c-1)}\setminus i}^+} \overline{q_i}(m, f_{g_i}^+, f_{g_1^{(c-1)}\setminus i}) \mathrm{d}m\mathrm{d}f_{g_1^{(c-1)}\setminus i} \right.$$

$$\left. - \frac{\mathrm{d}f_{g_1^{(c-1)}}^-}{\mathrm{d}t} \int_{m_k^-}^{m_k^+} \int_{f_{g_1^{(c-1)}\setminus i}^-}^{f_{g_1^{(c-1)}\setminus i}^+} \overline{q_i}(m, f_{g_i}^-, f_{g_1^{(c-1)}\setminus i}) \mathrm{d}m\mathrm{d}f_{g_1^{(c-1)}\setminus i} \right] \quad (15)$$

GMDD
7, 7937–7987, 2014

Substituting Eq. (A16) and $\overline{q_i} = m\ f_i\ \overline{n}$ into Eq. (15), we obtain:

$$\frac{\partial Q_i^j}{\partial t} = \overbrace{\int_{m_k^-}^{m_k^+}\int_{f_{g_1^{(c-1)}}^-}^{f_{g_1^{(c-1)}}^+} m\ f_{g_i}\frac{\partial \overline{n}}{\partial t}\mathrm{d}m\mathrm{d}f_{g_1^{(c-1)}}}^{C} + \int_{m_k^-}^{m_k^+}\int_{f_{g_1^{(c-1)}}^-}^{f_{g_1^{(c-1)}}^+} \overline{n}\ l_{g_i}\ \mathrm{d}m\mathrm{d}f_{g_1^{(c-1)}}$$

$$\overbrace{+ m_k^+\frac{\mathrm{d}m_k^+}{\mathrm{d}t}\int_{f_{g_1^{(c-1)}}^-}^{f_{g_1^{(c-1)}}^+} f_{g_i}\ \overline{n}(m_k^+, f_{g_1^{(c-1)}})\mathrm{d}f_{g_1^{(c-1)}} - m_k^-\frac{\mathrm{d}m_k^-}{\mathrm{d}t}\int_{f_{g_1^{(c-1)}}^-}^{f_{g_1^{(c-1)}}^+} f_{g_i}\ \overline{n}(m_k^-, f_{g_1^{(c-1)}})\mathrm{d}f_{g_1^{(c-1)}}}^{D}$$

$$+\sum_{i=1}^{(c-1)}\left[f_{g_i}^+\frac{\mathrm{d}f_{g_1^{(c-1)}}^+}{\mathrm{d}t}\int_{m_k^-}^{m_k^+}\int_{f_{g_1^{(c-1)}\setminus i}^-}^{f_{g_1^{(c-1)}\setminus i}^+} m\ \overline{n}(m, f_{g_i}^+, f_{g_1^{(c-1)}\setminus i})\mathrm{d}m\mathrm{d}f_{g_1^{(c-1)}\setminus i}\right.$$

$$\left.-f_{g_i}^-\frac{\mathrm{d}f_{g_1^{(c-1)}}^-}{\mathrm{d}t}\int_{m_k^-}^{m_k^+}\int_{f_{g_1^{(c-1)}\setminus i}^-}^{f_{g_1^{(c-1)}\setminus i}^+} m\ \overline{n}(m, f_{g_i}^-, f_{g_1^{(c-1)}\setminus i})\mathrm{d}m\mathrm{d}f_{g_1^{(c-1)}\setminus i}\right] \quad (16)$$

GMDD
7, 7937–7987, 2014

Similarly to Eq. (11), it can be proved that $C = -D$, so that Eq. (16) simplifies to:

$$\frac{\partial Q_i^j}{\partial t} = \int_{m_k^-}^{m_k^+} \int_{f_{g_1^{(c-1)}}^-}^{f_{g_1^{(c-1)}}^+} \overline{n}\, I_{g_i}\, \mathrm{d}m\mathrm{d}f_{g_1^{(c-1)}} = N^j\, I_{g_i} \tag{17}$$

Thus, in each section, the change with time of number and mass concentrations is given by Eqs. (14) and (17).

2.1.4 Numerical implementation

According to Debry and Sportisse (2006), the condensation/evaporation process may have characteristic time-scales of different magnitudes, because the range of particle diameters is large. Such feature induces strong stiffness of the numerical system. As suggested by Debry et al. (2007), the stiff condensation/evaporation equations are solved using the second-order Rosenbrock (ROS2) method (Verwer et al., 1999; Djouad et al., 2002).

In addition, potentially unstable oscillations may occur when a dramatic change of the particle pH occurs. To address this issue, a species flux electro-neutrality constraint (Pilinis et al., 2000; Debry et al., 2007) is applied in SCRAM to ensure the numerical stability of the system.

2.2 Bulk equilibrium and hybrid approaches

Bulk equilibrium methods assume an instantaneous thermodynamic equilibrium between the gas and bulk-aerosol phases. For semi-volatile species, the mass concentration of both gas and bulk-aerosol phases after condensation/evaporation are obtained using the forward mode of ISORROPIA for inorganic and the H_2O model (Couvidat et al., 2012) for organics. Because time integration is not necessary, the computational

GMDD
7, 7937–7987, 2014

cost is significantly reduced compared to the dynamic method. Weighting factors W are designed to distribute the semi-volatile bulk-aerosol mass across the aerosol distribution (Pandis et al., 1993). In SCRAM, for each semi-volatile species i, we redistribute the bulk aerosol evaporating or condensing mass, $\delta Q_i = Q_i^{\text{after bulk eq.}} - Q_i^{\text{before bulk eq.}}$, between the sections j, using factors that depend on the ratio of the mass transfer rate in the aerosol distribution (Eq. 2). Because of the bulk equilibrium assumption, the driving force of $(c_i^{\text{g}} - K_{\text{e}} c_i^{\text{eq}})$ is assumed to be the same for all size and composition sections, and the weighting factors are as follows.

$$W_i^j = \frac{N_j \; d_{\text{p}}^j f(Kn, \alpha_i)}{\sum_{k=1}^{N_s} N_k \; d_{\text{p}}^k f(Kn, \alpha_i)} \tag{18}$$

where N_j is the number concentration of section j and d_{p}^j is the particle wet diameter of section j. In case of evaporation, these weighting factors may not be appropriate, as they may lead to over-evaporation of some species in some sections, i.e. $Q_i^j = Q_i^{\text{before bulk eq.}} + \delta Q_i \times W_i^j < 0$. In the case of over-evaporation, we use a weighting scheme that redistributes the total bulk aerosol mass rather than the bulk aerosol evaporating or condensing mass

$$W_i^j = \frac{Q_i^j}{\sum_{k=1}^{N_s} Q_i^k} \tag{19}$$

and $Q_i^j = Q_i^{\text{after bulk eq.}} \times W_i^j$.

In fact, due to their larger ratios between surface area and particle mass, small particles may reach thermodynamic equilibrium much faster than large particles. Particles of diameters larger than 1 µm could require hours or even days to achieve equilibrium (Wexler and Seinfeld, 1990), which makes the bulk equilibrium assumption inappropriate for them. In order to maintain both the computational efficiency of the equilibrium

GMDD
7, 7937–7987, 2014

method and the accuracy of the dynamic one, a hybrid method is adopted in SCRAM based on the work of Capaldo et al. (2000) and Debry and Sportisse (2006). This method uses the equilibrium method for small particles ($d_p < 1\,\mu m$) and uses the dynamic method to calculate the mass transfer for larger particles.

2.3 Size and composition redistribution

By condensation/evaporation, the particles in each size section may grow or shrink. Because the bounds of size sections should be fixed for 3-D applications, it is necessary to redistribute number and mass among the fixed size sections during the simulation after condensation/evaporation. Similarly, the chemical composition also evolves by condensation/evaporation, and an algorithm is needed to identify the particle composition and redistribute it into the correct composition sections.

Two redistribution methods for size sections may be used in SCRAM: the HEMEN (Hybrid of Euler–Mass and Euler–Number) scheme of Devilliers et al. (2013) and the moving diameter scheme of Jacobson (1997). According to Devilliers et al. (2013), both redistribution methods may accurately redistribute mass and number concentrations.

The HEMEN scheme divides particle size sections into two parts: the number is redistributed for sections of mean diameter lower than 100 nm and mass is redistributed for sections of mean diameter greater than 100 nm. The section mean diameters are kept constant and mass concentrations are diagnosed for sections where number is redistributed, while number concentrations are diagnosed for sections where mass is redistributed. The advantage of this scheme is that it is more accurate for number concentrations over the size range where number concentrations are highest and more accurate for mass concentrations where mass concentrations are highest. In SCRAM, the algorithm of Devilliers et al. (2013) was modified to take into account the fact that after condensation/evaporation, the diameter of a section may become larger than the upper bound of the next section. This feature allows us to use larger time steps for condensation/evaporation before redistribution.

GMDD
7, 7937–7987, 2014

In the moving diameter method, although size section bounds are kept fixed, the representative diameter of each size section is allowed to vary. If, after condensation/evaporation, the diameter grows or shrinks outside section bounds, both the mass and number concentrations of the section are redistributed entirely into the new size sections bounding that diameter.

For the composition redistribution, a scheme based on the moving diameter method is applied. First, after condensation/evaporation, the mass fraction of each species is re-evaluated within each section. For each section, if the new composition does not match the section composition (i.e., if the mass fraction of each species does not fit into the mass fraction bounds of the species for that section), the section which has a composition that matches the new composition is identified, and both number and mass concentrations of each species are transferred to that section.

2.4 Time resolution of SCRAM

In order to develop a system that offers both computational efficiency and numerical stability, we perform operator splitting for changes in number and mass concentrations with time due to emission, coagulation, condensation/evaporation and nucleation, as explained below.

Emissions are first evaluated with an emission time step, which is determined by the characteristic time-scales of emissions obtained from the ratio of emission rates to aerosol concentrations. The emission time step evolves with time to prevent adding too much emitted mass into the system within one time step. Within each emission time step, coagulation and condensation/evaporation/nucleation are solved and the splitting time step between coagulation and condensation/evaporation/nucleation is forced to be lower than the emission time tep. Time steps are obtained from the characteristic time steps of coagulation (t_{coag}) and condensation/evaporation/nucleation (t_{cond}). The larger of the time steps t_{coag} and t_{cond} determines the time step of splitting between coagulation and condensation/evaporation/nucleation. As coagulation is usually the slower process, the change due to coagulation is first calculated over its time step.

GMDD
7, 7937–7987, 2014

Then, the change due to condensation/evaporation/nucleation is calculated, using time sub cycles, starting with the sub time step t_{cond}. The next sub time step for condensation/evaporation/nucleation is estimated based on the difference between the first and second order results provided by the ROS2 solver. Redistribution is computed after each time step of splitting of coagulation and condensation/evaporation/nucleation.

When the bulk thermodynamic equilibrium assumption is made, condensation/evaporation is computed with the bulk equilibrium method once per emission time step. In the case of a simulation with the hybrid method for condensation/evaporation, the change with time of the equilibrium size section is computed with a fixed time step of 600 s, which is larger than the emission time steps, so that enough time is available for the evolution between the background gas concentration and particle surface concentrations for each size section undergoing dynamic mass transfer. Redistribution is computed after each equilibrium time step.

3 Model validation

To validate the model, the change with time of internally- and externally-mixed aerosol models are compared. The simulations use initial conditions for number and mass concentrations that are typical of a regional haze scenario, with a sulphuric acid condensation rate of 5.5 $\mu m^3\,cm^{-3}$ per 12 h (Seigneur et al., 1986; Zhang et al., 1999).

Simulations were conducted for 12 h at a temperature of 298 K and a pressure of 1 ATM. The original reference simulation (Seigneur et al., 1986; Zhang et al., 1999) was first reproduced for internally-mixed sulphate particles (redistribution is not applied). For the sake of comparison between internally- and externally-mixed simulations, half of the particles were assumed to consist of sulphate (species 1) and the other half of another species of similar physical properties as sulphate (species 2). As both species have the same physical properties, for any given size section, the sum over all composition sections of number and mass concentrations of externally-mixed particles should equal the number and mass concentrations of the internally-mixed particles. Particles

GMDD
7, 7937–7987, 2014

were discretised into 100 size sections and 10 composition sections for the externally-mixed case. Figure 1 compares the initial mass distributions as a function of both particle size and species 1 mass fraction of the internally- and externally-mixed cases. Figure 2 shows the initial and final distributions for the number and volume concentrations as a function of particle diameters. Both the internally-mixed and externally-mixed results are presented in Fig. 2, along with the reference results of Zhang et al. (1999) (500 size sections were used in the original reference simulation). For the externally-mixed simulation, the results were summed up over composition sections to obtain the distributions as a function of particle diameter. As expected, a perfect match is obtained between internal and external mixing distributions, with a 100 % Pearson's correlation coefficient. Furthermore, the accuracy of the SCRAM algorithm is proved by the perfect match between the results of these simulations and the reference simulation of Zhang et al. (1999).

Using the same initial conditions and sulphuric acid condensation rate, a second comparison test was performed, with both coagulation and condensation occurring for 12 h. As the coagulation algorithm requires size sections to have fixed bounds (Dergaoui et al., 2013), size redistribution was applied for both the internally- and externally-mixed cases using the HEMEN method. As in the first comparison test, Fig. 3 shows that there is a perfect match between the internally- and externally-mixed distributions as a function of particle diameter (no reference simulation was available for these simulations). This test validates the algorithm of SCRAM to simulate jointly the coagulation and condensation of externally-mixed particles.

The mixing states of both internally- and externally-mixed particles at the end of the simulations of the second test are shown in Fig. 4. Sulphuric acid condenses to form particulate sulphate (species 1). During the simulation, pure species 2 particles mix with pure sulphate particles by coagulation and condensation of sulphuric acid. Figure 4 shows that, at the end of the simulation, the sulphate mass fraction is greater for particles of lower diameters, because the condensation rate is greater for those particles. Particles with diameters greater than 10 µm remain unmixed. However, the

GMDD
7, 7937–7987, 2014

external mixing state provides a more detailed mixing map, from which it is possible to distinguish mixed particles from unmixed ones and to trace the origin of each particle. In this test case where the effect of condensation dominates that of coagulation, most mixed particles are originally pure species 2 particles coated with newly condensed sulphuric acid (Fig. 4).

4 Simulation with realistic concentrations

To test the impact of external mixing on aerosol concentrations, simulations of coagulation, condensation/evaporation and nucleation were performed with SCRAM using realistic ambient concentrations and emissions extracted from a simulation performed over Greater Paris for July 2009 during the MEGAPOLI (Megacities: Emissions, urban, regional and Global Atmospheric POLution and climate effects, and Integrated tools for assessment and mitigation) campaign (Couvidat et al., 2013).

4.1 Simulation set-up

Data were extracted from one grid cell of the 3-D simulation performed by Couvidat et al. (2013) over Greater Paris. This surface grid cell was chosen because black carbon (BC) emissions are high in that location, due to high traffic emissions. Figure 5 shows the BC emission map at 02:00 UT, at 1 July 2009. The highest emission rate is located at the grid cell center of longitude and latitude (2.28, 48.88°), which was selected here to extract the SCRAM simulation input data for emissions, background gas and aerosol concentrations, and initial meteorological conditions (temperature and pressure). In the absence of specific information on individual particle composition, all initial aerosol concentrations extracted from the database were assumed to be 100 % mixed (i.e., aged background aerosols).

Simulations start at 02:00 UT (1 July 2009), i.e., just before the morning peak of traffic emissions, and last 12 h. As our simulations are 0-D, the transport of gases and

GMDD
7, 7937–7987, 2014

particles is not taken into account (i.e., one assume calm conditions). Therefore, emissions accumulate, potentially leading to unrealistically high concentrations. To avoid this artifact, the duration of the emissions was limited to the first 40 min of simulation. This time duration is calculated using the average BC emission rate between 02:00 and 03:00 UT, so that BC emissions lead to an increase in BC concentrations equal to the difference between BC concentrations after and before the morning traffic peak, i.e., between 06:00 and 02:00 UT (Fig. 6).

The size distribution ranging from 0.001 to 10 µm was discretised into 7 sections with bounds at 0.001, 0.005, 0.01, 0.0398, 0.1585, 0.6310, 2.5119, and 10 µm. As in Couvidat et al. (2013), 31 particulate species were included in our simulations. In order to reduce the computational cost of the externally-mixed simulations, these species were grouped into 5 groups based on their chemical nature: the hydrophilic inorganic group (HLI) contains five inorganic species (sodium, sulphate, nitrate, ammonium and chloride); the hydrophilic organic group (HLO) contains 9 hydrophilic surrogate organic species (BiA2D, BiA1D, BiA0D, GLYOXAL, MGLY, BiMT, BiPER, BiDER and BiMGA); the hydrophobic organic group (HBO) contains 14 hydrophobic surrogate organic species (AnBlP, AnBmP, BiBlP, BiBmP, BiNGA, NIT3, BiNIT, AnCLP, SOAlP, SOAmP, SOAhP, POAlP, POAmP and POAhP); the black carbon group (BC) contains only black carbon; and the dust group (DU) contains all the neutral particles made up of soil, dust and fine sand. Refer to Couvidat et al. (2012) for detailed nomenclature of the organic species. For each of the first four groups, the mass fraction of the group over the total mass is discretised into 3 mass fraction sections ($[0.0, 0.2), (0.2, 0.8], (0.8, 1.0]$), leading to 20 possible particle composition sections, as shown in Table 1. Among them, there are 5 unmixed particles and 15 mixed particles. The dust mass fraction is not discretised, as it is obtained by mass conservation. In each group, water may also be present, although it is not considered when computing the mass fractions (it is calculated separately with the thermodynamic equilibrium models).

GMDD
7, 7937–7987, 2014

4.2 Aerosol dynamics and mixing state

To understand how initial concentrations mix with emissions, four scenarios were simulated. In the scenario a, only emissions are taken into account in the simulation. Only coagulation is added to emissions in scenario b, while only condensation/evaporation is added to emissions in scenario c. In the scenario d, emissions and all the aerosol dynamic processes are taken into account including nucleation (however, nucleation was not activated during the simulation due to low sulphuric acid gas concentrations).

The mass and number distributions of each chemical composition after 12 h simulation are shown in Figs. 7 and 8 as a function of particle diameter. Bars with grayscale represent unmixed particles, while bars with colours are mixed particles. Each bar corresponds to a chemical composition index (CI). The chemical compositions and the CI value associated with color bars are listed in Table 1.

As shown by the simulation of scenario a, emissions lead to high number concentrations of BC in the sections of low diameters (mostly below 0.631 µm) and to high mass concentrations of dust and BC in the sections of high diameters (mostly above 0.631 µm).

The comparison of scenarios a and b shows that coagulation does not affect much mass concentrations, but significantly reduces the number concentrations of particles in the sections of diameters lower than 0.631 µm. Also, due to coagulation, particles migrated to higher sections. For example, this is illustrated by mixed particles of CI 15 that migrated from the third size section to the fourth size section (see Fig. 8).

As shown by the simulation of scenario c, condensation/evaporation leads to high mass and number concentrations of unmixed HBO (CI 6 – mass fraction of HBO above 80 %), increasing the amount of unmixed particles. Organic matter of low and medium volatilities is emitted in the gas phase following Couvidat et al. (2013). This organic matter condenses subsequently on well-mixed particles (CI 14 with mixed HLI and HBO), in sufficient amount to increase the mass fraction of HBO to over 80 % and, therefore, transferring particles to the unmixed category CI 6 (these particle are not exactly un-

GMDD
7, 7937–7987, 2014

mixed since up to 20 % may correspond to HLI, but a finer composition resolution would be required to analyse their mixed characteristics). The condensation of organic matter on freshly emitted BC particles also occurs. Mixed BC and HBO particles (CI 5) appear in the third and fourth size sections.

As shown by comparing scenarios a and b and scenarios c and d, coagulation significantly reduces number concentrations. The mass concentrations of fine particles (diameters lower than 0.631 µm) are also reduced. Furthermore, the composition diversity increases. For example, newly mixed particles of CI 4 (between 20 and 80 % of HBO) are formed by the coagulation of unmixed particles from CI 6 with others within the fourth and fifth size sections.

Table 2 shows the percentage of mixed particles for each scenario based on both particle number and mass concentrations. In general, the mixed particle percentages based on mass are higher than those based on number. This indicates that large particles, which dominate the mass concentrations, are better mixed than small particles, which dominate the number concentrations. The reason of this difference of mixing state between large and small particles is that emissions lead to high number concentrations of unmixed small particles.

The number/mass mixing percentages after emission only (scenario a) provide a baseline for the analysis of the three other scenarios. In scenario a, 42 % (resp. 83 %) of mixed particles number (resp. mass) concentration originates from initial conditions, while the remaining unmixed particles are due to emissions. The comparison of scenarios a and b shows that coagulation increases the mixing percentages, especially for small particles of high number concentrations. The mass mixing percentages decrease in scenario c because the condensation of freshly emitted organic matter on large mixed particles leads to particles with a mass fraction of organic matter (HBO) higher than 80 %, i.e. unmixed. When all aerosol dynamic processes are taken into account (scenario d), only 51 % of particle number concentration and 76 % of particle mass concentration are mixed. The mixing percentages are greater than those of scenario c, as mixing increases by coagulation, but the mass mixing percentage is lower

GMDD
7, 7937–7987, 2014

than in scenario a (emissions only) because of the strong condensation of HBO emitted in the gas phase.

4.3 External vs. internal mixing

To investigate the consequence of the internal mixing hypothesis, a simulation of scenario d (all aerosol dynamic processes are taken into account) is conducted by assuming all particles to be internally mixed. Externally- and internally-mixed 12 h simulations lead to a similar total aerosol mass concentration after 12 h (33.09 $\mu g\,m^{-3}$ for internal mixing and 33.35 $\mu g\,m^{-3}$ for external mixing) as well as to similar total number concentrations ($1.16 \times 10^{10}\,\#\,m^{-3}$ for internal mixing and $1.07 \times 10^{10}\,\#\,m^{-3}$ for external mixing). The number and the species mass distributions are also similar, although external mixing leads to slightly lower ammonium concentrations (2.68 $\mu g\,m^{-3}$ vs. 2.70 $\mu g\,m^{-3}$), slightly higher nitrate concentrations (3.19 $\mu g\,m^{-3}$ vs. 3.03 $\mu g\,m^{-3}$) and higher chloride concentrations (0.36 $\mu g\,m^{-3}$ vs. 0.25 $\mu g\,m^{-3}$).

Figure 11 compares the mass distributions and compositions within each size section after 12 h of the internal and external mixing simulations. External mixing provides more detail about the particle mixing state, as within each size section particles have different compositions. For example, in the case of internal mixing, particles in size Sect. 4 (diameter between 0.0398 and 0.1585 µm) are all mostly hydrophobic organics (CI 4: HBO between 20 and 80 %). The particle compositions are more detailed in the external mixing simulation: while less than half of the particles are mostly hydrophobic organics (CI 4) as in internal mixing, a large amount are unmixed particles (TI6: HBO between 80 and 100 %), and some are equally mixed with inorganic and hydrophobic organics (CI 5). In size Sect. 5, as in the internal mixing simulation, mixed particles dominate (CI 14), but many have a different composition (CI 4 and 5) and some are unmixed HBO (CI 6), BC (CI 3) and dust (CI 1). For particles in size Sect. 6, particles are mixed particles of CI 12, while external mixing also shows that some particles are unmixed (BC (CI 3) and dust (CI 1)) and there are CI 14 particles that originated from size Sect. 5 through coagulation.

GMDD
7, 7937–7987, 2014

4.4 Bulk equilibrium and hybrid approaches

Additional external mixing tests were conducted using the bulk equilibrium and hybrid approaches for condensation/evaporation to evaluate both their accuracy and computational efficiency. In the hybrid approach, the lowest four sections are assumed to be at equilibrium (up to diameters of 0.1585 µm), whereas the other sections undergo dynamic mass transfer between the gas and particle phases.

The accuracy of these approaches is evaluated by comparing the mass and number distributions after 12 h simulations with the bulk equilibrium or the hybrid approaches to the mass and number distributions computed dynamically (see Figs. 9 and 10).

For externally-mixed particles, the dynamic mass distribution is shown in Fig. 7c; the bulk equilibrium and hybrid mass distributions are shown in Fig. 9a and c, respectively. The dynamic number distribution is shown in Fig. 8c; the bulk equilibrium and hybrid mass distributions are shown in Fig. 10a and c, respectively. For internally mixed particles, the dynamic mass/number distributions are shown in Figs. 9d and 10d and the bulk equilibrium mass/number distributions in Figs. 9b and 10b, respectively.

For internally-mixed particles, the comparisons between Fig. 9b and d and between Fig. 10b and d indicate that the bulk equilibrium approach leads to significantly different distributions and compositions than the dynamic approach. This result also holds for externally-mixed particles, as shown by the comparisons between Fig. 7c and a and between Figs. 8c and 10a. For example, more inorganic species condense on particles in the fourth size section (between 0.0.0398 and 0.1585 µm) in the case of bulk equilibrium compared to the fully dynamic case. This section is dominated by CI 14 (equal mixture of inorganic and hydrophobic organics) for bulk equilibrium, instead of CI 6 (unmixed hydrophobic organics) for dynamic. Internal and external distributions are similar with the dynamic approach, as well as with the bulk equilibrium approach. Although internal and external compositions are different with the dynamic approach, they are quite similar with the bulk equilibrium approach. However, with the bulk equilib-

GMDD
7, 7937–7987, 2014

rium approach, similarly to the dynamic approach, unmixed particles of CI 3 (unmixed BC) remain present in most size sections for externally-mixed particles.

The mass and number distributions and compositions obtained with the hybrid approach are similar to the fully dynamic approach. For example, the over-condensation of inorganic species in the fourth size section (leading to particles of CI 14 with bulk equilibrium) is restrained with the hybrid approach, as the fourth size section is computed dynamically, and particles consist of CI 6, as with the dynamic approach.

Table 3 shows the computational times (CPU) required for each simulation on a DELL Precision T3500 workstation (lowest integration time step: 1). External mixing requires more CPU, especially for computing coagulation and dynamic condensation/evaporation (C/E). The largest difference between internal and external mixing occurs for computing coagulation, which is almost 800 times slower with external mixing. Bulk equilibrium C/E provides a huge economy in CPU time for all simulations compared to dynamic C/E, while the computational advantage of hybrid C/E is more obvious for internal mixing (17 times faster than dynamic C/E) than external mixing (15 % times faster than dynamic C/E).

5 Conclusions

A new Size-Composition Resolved Aerosol Model (SCRAM) has been developed to simulate the dynamic evolution of externally-mixed particles due to coagulation, condensation/evaporation, and nucleation. The general dynamic equation is discretised for both size and composition. Particle compositions are represented by the combinations of mass fractions which may be chosen to correspond either to the mass fraction of the different species or to the mass fraction of groups of species (e.g. inorganic, hydrophobic organics. . .). The total numbers and bounds of the size and composition sections are defined by the user. An automatic classification method is designed within the system to determine all the possible particle compositions based on the combinations of user-defined chemical species or groups and their mass-fraction sections.

GMDD
7, 7937–7987, 2014

The model was first validated by comparison to internally-mixed simulations of condensation/evaporation of sulphuric acid and of condensation/evaporation of sulphuric acid with coagulation. It was also validated for condensation against a reference solution.

The model was applied using realistic concentrations and emissions typical of air pollution over Greater Paris, where traffic emissions are high. Initial concentrations were assumed to be internally mixed. Simulations lasted 12 h.

Although internally- and externally-mixed simulations lead to similar particle size distributions, the particle compositions are different. The externally-mixed simulations offer more detail about particle mixing states within each size section when compared to internally mixed simulations. After 12 h, 49 % of number concentrations and 24 % of mass concentrations are not mixed. These percentages may be higher in 3-D simulations, because initial aerosol concentrations should not be assumed as entirely internally mixed over an urban area. Coagulation is quite efficient at mixing particles, as 52 % of number concentrations and 36 % of mass concentrations are not mixed if coagulation is not taken into account in the simulation. On the opposite, condensation may decrease the percentage of mixed particles when low-volatility gaseous emissions are high.

Assuming bulk equilibrium when solving condensation/evaporation leads to different distributions and compositions than the dynamic approach under both the internally- and externally-mixed assumptions. Although internally- and externally-mixed assumptions lead to similar compositions with the bulk equilibrium approach, unmixed particles remain when particles are externally mixed, similarly to the dynamic approach.

Future work will focus on the incorporation of SCRAM into the air quality modelling platform Polyphemus for 3-D simulations. In order to investigate its performance in modelling air quality over Greater Paris, model simulation results will be compared to observations (Healy et al., 2012).

GMDD
7, 7937–7987, 2014

Code availability

The SCRAM source code related to this article is available from the web page: http://cerea.enpc.fr/scram/index.html.

SCRAM is a free software. You can redistribute it and/or modify it under the terms of the GNU General Public License as published by the Free Software Foundation.

Appendix A: Change of variables for the evolution of number and mass distributions

This appendix describes how to derive the equations of change for the number concentration $\overline{n}$ and mass concentration $\overline{q}$ distributions as a function of the variables $f_1, \ldots, f_{(c-1)}, m$ used in the external mixing formulation.

To derive the equation of change for $\overline{n}(f_1, \ldots, f_{(c-1)}, m)$ (Eq. 5) from the equation of change for $n(m_1, \ldots, m_c)$ (Eq. 1), we need to perform a change of variables from $m_1, \ldots, m_c$ to $f_1, \ldots, f_{(c-1)}, m$ and to compute the $[c \times c]$ Jacobian Matrix

GMDD
7, 7937–7987, 2014

$$\mathbf{J}(f_1, f_2, \cdots, f_{(c-1)}, m)$$

$$\mathbf{J} = \begin{bmatrix} \frac{\partial m_1}{\partial f_1} & \frac{\partial m_1}{\partial f_2} & \cdots & \frac{\partial m_1}{\partial f_{(c-1)}} & \frac{\partial m_1}{\partial m} \\ \frac{\partial m_2}{\partial f_1} & \frac{\partial m_2}{\partial f_2} & \cdots & \frac{\partial m_2}{\partial f_{(c-1)}} & \frac{\partial m_2}{\partial m} \\ \vdots & \vdots & \ddots & \vdots & \vdots \\ \frac{\partial m_{(c-1)}}{\partial f_1} & \frac{\partial m_{(c-1)}}{\partial f_2} & \cdots & \frac{\partial m_{(c-1)}}{\partial f_{(c-1)}} & \frac{\partial m_{(c-1)}}{\partial m} \\ \frac{\partial m_c}{\partial f_1} & \frac{\partial m_c}{\partial f_2} & \cdots & \frac{\partial m_c}{\partial f_{(c-1)}} & \frac{\partial m_c}{\partial m} \end{bmatrix}$$

$$= \begin{bmatrix} m & 0 & \cdots & 0 & f_1 \\ 0 & m & \cdots & 0 & f_2 \\ \vdots & \vdots & \ddots & \vdots & \vdots \\ 0 & 0 & \cdots & m & f_{(c-1)} \\ -m & -m & \cdots & -m & 1 - \sum_{i=1}^{(c-1)} f_i \end{bmatrix} \quad \text{(A1)}$$

and the Jacobian inverse matrix:

$$\mathbf{J}^{-1} = \begin{bmatrix} \frac{1-f_1}{m} & -\frac{f_1}{m} & \cdots & -\frac{f_1}{m} & -\frac{f_1}{m} \\ -\frac{f_2}{m} & \frac{1-f_2}{m} & \cdots & -\frac{f_2}{m} & -\frac{f_2}{m} \\ \vdots & \vdots & \ddots & \vdots & \vdots \\ -\frac{f_{(c-1)}}{m} & -\frac{f_{(c-1)}}{m} & \cdots & \frac{1-f_{(c-1)}}{m} & -\frac{f_{(c-1)}}{m} \\ 1 & 1 & \cdots & 1 & 1 \end{bmatrix} \quad \text{(A2)}$$

The relationship between n and $\overline{n}$ is

$$n = \frac{\overline{n}}{\det(J)} = \frac{\overline{n}}{m^{(c-1)}} \quad \text{(A3)}$$

GMDD
7, 7937–7987, 2014




Thus,

$$\frac{\partial n}{\partial t} = \frac{\partial \left(\frac{\overline{n}}{m^{(c-1)}}\right)}{\partial t} = \frac{1}{m^{(c-1)}} \frac{\partial \overline{n}}{\partial t} \tag{A4}$$

For the right-hand side of Eq. (1), the terms $\frac{\partial (l_i n)}{\partial m_i}$ are replaced by terms depending on the new variables, using:

$$\left(\frac{\partial (l_1 n)}{\partial m_1}, \frac{\partial (l_2 n)}{\partial m_2}, \cdots, \frac{\partial (l_c n)}{\partial m_c}\right) = \left(\frac{\partial (l_1 n)}{\partial f_1}, \frac{\partial (l_2 n)}{\partial f_2}, \cdots, \frac{\partial (l_{(c-1)} n)}{\partial f_{(c-1)}}, \frac{\partial (l_c n)}{\partial m}\right) \times \mathbf{J}^{-1} \tag{A5}$$

For $i \in (1, (c-1))$, this leads to:

$$\frac{\partial (l_i n)}{\partial m_i} = \frac{1}{m} \frac{\partial (l_i n)}{\partial f_i} - \sum_{j=1}^{(c-1)} \frac{f_j}{m} \frac{\partial (l_i n)}{\partial f_j} + \frac{\partial (l_i n)}{\partial m} \tag{A6}$$

and for $i = c$:

$$\frac{\partial (l_c n)}{\partial m_c} = - \sum_{j=1}^{(c-1)} \frac{f_j}{m} \frac{\partial (l_c n)}{\partial f_j} + \frac{\partial (l_c n)}{\partial m} \tag{A7}$$

If we replace l_c with $l_0 - \sum_{i=1}^{(c-1)} l_i$ in (A7), we have:

$$\frac{\partial (l_c n)}{\partial m_c} = - \sum_{j=1}^{(c-1)} \frac{f_j}{m} \frac{\partial (l_0 n)}{\partial f_j} + \sum_{i=1}^{(c-1)} \sum_{j=1}^{(c-1)} \frac{f_j}{m} \frac{\partial (l_i n)}{\partial f_j} + \frac{\partial (l_0 n)}{\partial m} - \sum_{i=1}^{(c-1)} \frac{\partial (l_i n)}{\partial m} \tag{A8}$$

The sum of the first $(c-1)$ terms of the right side of Eq. (1) may be written as follows.

$$\sum_{i=1}^{(c-1)} \frac{\partial (l_i n)}{\partial m_i} = \frac{1}{m} \sum_{i=1}^{(c-1)} \frac{\partial (l_i n)}{\partial f_i} - \sum_{i=1}^{(c-1)} \sum_{j=1}^{(c-1)} \frac{f_j}{m} \frac{\partial (l_i n)}{\partial f_j} + \sum_{i=1}^{(c-1)} \frac{\partial (l_i n)}{\partial m} \tag{A9}$$

GMDD
7, 7937–7987, 2014

The right-hand side of Eq. (1) becomes

$$-\sum_{i=1}^{c}\frac{\partial(I_i n)}{\partial m_i} = -\sum_{i=1}^{(c-1)}\frac{\partial(I_i n)}{\partial m_i} - \frac{\partial(I_c n)}{\partial m_c} = -\frac{1}{m}\sum_{i=1}^{(c-1)}\frac{\partial(I_i n)}{\partial f_i} + \sum_{i=1}^{(c-1)}\frac{f_i}{m}\frac{\partial(I_0 n)}{\partial f_i} - \frac{\partial(I_0 n)}{\partial m} \tag{A10}$$

If we denote $H_i = \frac{\partial f_i}{\partial t}$, then I_i may be written as follows.

$$I_i = \frac{\partial m_i}{\partial t} = \frac{\partial(m f_i)}{\partial t} = m\frac{\partial f_i}{\partial t} + f_i\frac{\partial m}{\partial t} = mH_i + f_i I_0 \tag{A11}$$

Replacing I_i by Eq. (A11) in Eq. (A10) and using $\frac{\partial m}{\partial f_i} = 0$,

$$\begin{aligned}-\sum_{i=1}^{c}\frac{\partial(I_i n)}{\partial m_i} &= -\frac{1}{m}\sum_{i=1}^{(c-1)}\frac{\partial(mH_i n + f_i I_0 n)}{\partial f_i} + \sum_{i=1}^{(c-1)}\frac{f_i}{m}\frac{\partial(I_0 n)}{\partial f_i} - \frac{\partial(I_0 n)}{\partial m} \\ &= -\sum_{i=1}^{(c-1)}\frac{\partial(H_i n)}{\partial f_i} - \frac{(c-1)}{m} I_0 n - \frac{\partial(I_0 n)}{\partial m}\end{aligned} \tag{A12}$$

Replacing n with $\frac{\overline{n}}{m^{(c-1)}}$ in Eq. (1) and using Eq. (A12), we have

$$\begin{aligned}\frac{1}{m^{(c-1)}}\frac{\partial\overline{n}}{\partial t} &= -\sum_{i=1}^{(c-1)}\frac{\partial(H_i\frac{\overline{n}}{m^{(c-1)}})}{\partial f_i} - \frac{(c-1)}{m^c} I_0\overline{n} - \frac{\partial(I_0\frac{\overline{n}}{m^{(c-1)}})}{\partial m} \\ &= -\frac{1}{m^{(c-1)}}\sum_{i=1}^{(c-1)}\frac{\partial(H_i\overline{n})}{\partial f_i} - \frac{1}{m^{(c-1)}}\frac{\partial(I_0\overline{n})}{\partial m}\end{aligned} \tag{A13}$$

and the equation of change for $\overline{n}$ is finally

$$\frac{\partial\overline{n}}{\partial t} = -\sum_{i=1}^{(c-1)}\frac{\partial(H_i\overline{n})}{\partial f_i} - \frac{\partial(I_0\overline{n})}{\partial m} \tag{A14}$$

GMDD
7, 7937–7987, 2014

The equation of change for the mass distribution $q_i = n\,m_i$ of species i is derived as follows.

$$\frac{\partial q_i}{\partial t} = \frac{\partial n\ m_i}{\partial t} = -m_i \frac{\partial n}{\partial t} + n\ I_i \tag{A15}$$

And the equation of change for $\overline{q}_i$ is obtained using $n = \frac{\overline{n}}{m^{(c-1)}}$, $q_i = \frac{\bar{q}_i}{m^{(c-1)}}$ and $m_i = m\ f_i$

$$\frac{\partial \overline{q_i}}{\partial t} = -m\ f_i \frac{\partial \overline{n}}{\partial t} + \overline{n}\ I_i \tag{A16}$$

Acknowledgements. The authors gratefully acknowledge Hilel Dergaoui (INRA) for providing his original code of coagulation process and Edouard Debry (INERIS) for optimizing the computation of coagulation repartition coefficients. We also would like to thank Florian Couvidat (INERIS) for his support on the implementation of his H_2O model into SCRAM as well as Stéphanie Deschamps (CEREA) who helped to improve the size redistribution algorithm.

References

Binkowski, F. S. and Roselle, S. J.: Models-3 Community Multiscale Air Quality (CMAQ) model aerosol component 1. Model description, J. Geophys. Res.-Atmos., 108, 4183, doi:10.1029/2001JD001409, 2003. 7938

Capaldo, K., Pilinis, C., and Pandis, S. N.: A computationally efficient hybrid approach for dynamic gas/aerosol transfer in air quality models, Atmos. Environ., 34, 3617–3627, 2000. 7953

Couvidat, F., Debry, É., Sartelet, K., and Seigneur, C.: A hydrophilic/hydrophobic organic (H2O) aerosol model: development, evaluation and sensitivity analysis, J. Geophys. Res.-Atmos., 117, D10304, doi:10.1029/2011JD017214, 2012. 7951, 7958

Couvidat, F., Kim, Y., Sartelet, K., Seigneur, C., Marchand, N., and Sciare, J.: Modeling secondary organic aerosol in an urban area: application to Paris, France, Atmos. Chem. Phys., 13, 983–996, doi:10.5194/acp-13-983-2013, 2013. 7957, 7958, 7959

Dahneke, B.: Simple kinetic theory of Brownian diffusion in vapors and aerosols, in: Theory of Dispersed Multiphase Flow, Academic Press, 97–133, 1983. 7942

GMDD

7, 7937–7987, 2014

Deboudt, K., Flament, P., Choël, M., Gloter, A., Sobanska, S., and Colliex, C.: Mixing state of aerosols and direct observation of carbonaceous and marine coatings on African dust by individual particle analysis, J. Geophys. Res.-Atmos., 115, D24207, doi:10.1029/2010JD013921, 2010. 7939

Debry, E. and Sportisse, B.: Reduction of the condensation/evaporation dynamics for atmospheric aerosols: Theoretical and numerical investigation of hybrid methods, J. Aerosol Sci., 37, 950–966, 2006. 7951, 7953

Debry, E., Fahey, K., Sartelet, K., Sportisse, B., and Tombette, M.: Technical Note: A new SIze REsolved Aerosol Model (SIREAM), Atmos. Chem. Phys., 7, 1537–1547, doi:10.5194/acp-7-1537-2007, 2007. 7941, 7951

Dergaoui, H., Sartelet, K. N., Debry, É., and Seigneur, C.: Modeling coagulation of externally mixed particles: Sectional approach for both size and chemical composition, J. Aerosol Sci., 58, 17–32, 2013. 7940, 7941, 7943, 7956

Devilliers, M., Debry, É., Sartelet, K., and Seigneur, C.: A new algorithm to solve condensation/evaporation for ultra fine, fine, and coarse particles, J. Aerosol Sci., 55, 116–136, 2013. 7953

Djouad, R., Sportisse, B., and Audiffren, N.: Numerical simulation of aqueous-phase atmospheric models: use of a non-autonomous Rosenbrock method, Atmos. Environ., 36, 873–879, 2002. 7951

EPA: Integrated Science Assessment for Particulate Matter, US Environmental Protection Agency, Washington, DC, 2009. 7938

Gelbard, F. and Seinfeld, J. H.: Simulation of multicomponent aerosol dynamics, J. Colloid Interf. Sci., 78, 485–501, 1980. 7938

Healy, R. M., Sciare, J., Poulain, L., Kamili, K., Merkel, M., Müller, T., Wiedensohler, A., Eckhardt, S., Stohl, A., Sarda-Estève, R., McGillicuddy, E., O'Connor, I. P., Sodeau, J. R., and Wenger, J. C.: Sources and mixing state of size-resolved elemental carbon particles in a European megacity: Paris, Atmos. Chem. Phys., 12, 1681–1700, doi:10.5194/acp-12-1681-2012, 2012. 7939, 7964

Hughes, L. S., Allen, J. O., Bhave, P., Kleeman, M. J., Cass, G. R., Liu, D.-Y., Fergenson, D. P., Morrical, B. D., and Prather, K. A.: Evolution of atmospheric particles along trajectories crossing the Los Angeles basin, Environ. Sci. Technol., 34, 3058–3068, 2000. 7939

GMDD
7, 7937–7987, 2014

Jacobson, M.: Analysis of aerosol interactions with numerical techniques for solving coagulation, nucleation, condensation, dissolution, and reversible chemistry among multiple size distributions, J. Geophys. Res., 107, 1327–1338, 2002. 7940

Jacobson, M. Z.: Development and application of a new air pollution modeling system – II. Aerosol module structure and design, Atmos. Environ., 31, 131–144, 1997. 7953

Jacobson, M. Z.: Strong radiative heating due to the mixing state of black carbon in atmospheric aerosols, Nature, 409, 695–697, 2001. 7939

Jacobson, M. Z., Turco, R. P., Jensen, E. J., and Toon, O. B.: Modeling coagulation among particles of different composition and size, Atmos. Environ., 28, 1327–1338, 1994. 7940

Kleeman, M. J. and Cass, G. R.: A 3-D Eulerian source-oriented model for an externally mixed aerosol, Environ. Sci. Technol., 35, 4834–4848, 2001. 7939

Kleeman, M. J., Cass, G. R., and Eldering, A.: Modeling the airborne particle complex as a source-oriented external mixture, J. Geophys. Res.-Atmos., 102, 21355–21372, 1997. 7939

Leck, C. and Svensson, E.: Importance of aerosol composition and mixing state for cloud droplet activation in the high Arctic, Atmos. Chem. Phys. Discuss., 14, 21223–21283, doi:10.5194/acpd-14-21223-2014, 2014. 7939

Lesins, G., Chylek, P., and Lohmann, U.: A study of internal and external mixing scenarios and its effect on aerosol optical properties and direct radiative forcing, J. Geophys. Res.-Atmos., 107, 4094, doi:10.1029/2001JD000973, 2002. 7939

Lu, J. and Bowman, F. M.: A detailed aerosol mixing state model for investigating interactions between mixing state, semivolatile partitioning, and coagulation, Atmos. Chem. Phys., 10, 4033–4046, doi:10.5194/acp-10-4033-2010, 2010. 7940

Mallet, M., Roger, J., Despiau, S., Putaud, J., and Dubovik, O.: A study of the mixing state of black carbon in urban zone, J. Geophys. Res.-Atmos., 109, D04202, doi:10.1029/2003JD003940, 2004. 7939

McMurry, P. H.: A review of atmospheric aerosol measurements, Atmos. Environ., 34, 1959–1999, 2000. 7939

Myhre, G., Samset, B. H., Schulz, M., Balkanski, Y., Bauer, S., Berntsen, T. K., Bian, H., Bellouin, N., Chin, M., Diehl, T., Easter, R. C., Feichter, J., Ghan, S. J., Hauglustaine, D., Iversen, T., Kinne, S., Kirkevåg, A., Lamarque, J.-F., Lin, G., Liu, X., Lund, M. T., Luo, G., Ma, X., van Noije, T., Penner, J. E., Rasch, P. J., Ruiz, A., Seland, Ø., Skeie, R. B., Stier, P., Takemura, T., Tsigaridis, K., Wang, P., Wang, Z., Xu, L., Yu, H., Yu, F., Yoon, J.-H., Zhang, K.,

GMDD
7, 7937–7987, 2014

Zhang, H., and Zhou, C.: Radiative forcing of the direct aerosol effect from AeroCom Phase II simulations, Atmos. Chem. Phys., 13, 1853–1877, doi:10.5194/acp-13-1853-2013, 2013. 7938

Nenes, A., Pandis, S. N., and Pilinis, C.: ISORROPIA: A new thermodynamic equilibrium model for multiphase multicomponent inorganic aerosols, Aquat. Geochem., 4, 123–152, 1998. 7943

Oshima, N., Koike, M., Zhang, Y., Kondo, Y., Moteki, N., Takegawa, N., and Miyazaki, Y.: Aging of black carbon in outflow from anthropogenic sources using a mixing state resolved model: model development and evaluation, J. Geophys. Res.-Atmos., 114, D06210, doi:10.1029/2008JD010680, 2009. 7940

Pandis, S. N., Wexler, A. S., and Seinfeld, J. H.: Secondary organic aerosol formation and transport – II. Predicting the ambient secondary organic aerosol size distribution, Atmos. Environ., 27, 2403–2416, 1993. 7952

Pascal, M., Corso, M., Chanel, O., Declercq, C., Badaloni, C., Cesaroni, G., Henschel, S., Meister, K., Haluza, D., Martin-Olmedo, P., Medinaa, S., and on behalf of the Aphekom group: Assessing the public health impacts of urban air pollution in 25 European cities: results of the Aphekom project, Sci. Total Environ., 449, 390–400, doi:10.1016/j.scitotenv.2013.01.077, 2013. 7938

Pilinis, C., Capaldo, K., Nenes, A., and Pandis, S.: MADM-A new multicomponent aerosol dynamics model, Aerosol Sci. Tech., 32, 482–502, 2000. 7951

Riemer, N., West, M., Zaveri, R. A., and Easter, R. C.: Simulating the evolution of soot mixing state with a particle-resolved aerosol model, J. Geophys. Res., 114, D09202, doi:10.1029/2008JD011073, 2009. 7939, 7942

Sartelet, K., Debry, E., Fahey, K., Roustan, Y., Tombette, M., and Sportisse, B.: Simulation of aerosols and gas-phase species over Europe with the Polyphemus system: Part I Model-to-data comparison for 2001, Atmos. Environ., 41, 6116–6131, 2007. 7938

Seigneur, C., Hudischewskyj, a. B., Seinfeld, J. H., Whitby, K. T., Whitby, E. R., Brock, J. R., and Barnes, H. M.: Simulation of aerosol dynamics: a comparative review of mathematical models, Aerosol Sci. Tech., 5, 205–222, 1986. 7955

Vehkamäki, H., Kulmala, M., Napari, I., Lehtinen, K. E., Timmreck, C., Noppel, M., and Laaksonen, A.: An improved parameterization for sulfuric acid–water nucleation rates for tropospheric and stratospheric conditions, J. Geophys. Res.-Atmos., 107, 4622, doi:10.1029/2002JD002184, 2002. 7941

GMDD
7, 7937–7987, 2014

Verwer, J. G., Spee, E., Blom, J., and Hundsdorfer, W.: A second-order Rosenbrock method applied to photochemical dispersion problems, SIAM J. Sci. Comput., 20, 1456–1480, 1999. 7951

Wexler, A. S. and Seinfeld, J. H.: The distribution of ammonium salts among a size and composition dispersed aerosol, Atmos. Environ., 24, 1231–1246, 1990. 7952

Whitby, E. R. and McMurry, P. H.: Modal aerosol dynamics modeling, Aerosol Sci. Tech., 27, 673–688, 1997. 7938

Zhang, Y., Seigneur, C., Seinfeld, J. H., Jacobson, M. Z., and Binkowski, F. S.: Simulation of Aerosol Dynamics: A Comparative Review of Algorithms Used in Air Quality Models, Aerosol Sci. Tech., 31, 487–514, 1999. 7955, 7956

Zhang, Y., Pun, B., Vijayaraghavan, K., Wu, S.-Y., Seigneur, C., Pandis, S. N., Jacobson, M. Z., Nenes, A., and Seinfeld, J. H.: Development and application of the model of aerosol dynamics, reaction, ionization, and dissolution (MADRID), J. Geophys. Res.-Atmos., 109, D01202, doi:10.1029/2003JD003501, 2004. 7938

Zhang, Y., McMurry, P. H., Yu, F., and Jacobson, M. Z.: A comparative study of nucleation parameterizations: 1. Examination and evaluation of the formulations, J. Geophys. Res.-Atmos., 115, D20212, doi:10.1029/2010JD014150, 2010. 7941

GMDD
7, 7937–7987, 2014

Table 1. 20 externally-mixed particle compositions.

Composition Index	Mixing state	Mass fraction of each groups (%)				
		HLI	HLO	HBO	BC	DU
1	unmixed(DU)	0–20	0–20	0–20	0–20	0–100
2	mixed	0–20	0–20	0–20	20–80	0–100
3	unmixed(BC)	0–20	0–20	0–20	80–100	0–100
4	mixed	0–20	0–20	20–80	0–20	0–100
5	mixed	0–20	0–20	20–80	20–80	0–100
6	unmixed(HBO)	0–20	0–20	80–100	0–20	0–100
7	mixed	0–20	20–80	0–20	0–20	0–100
8	mixed	0–20	20–80	0–20	20–80	0–100
9	mixed	0–20	20–80	20–80	0–20	0–100
10	mixed	0–20	20–80	20–80	20–80	0–100
11	unmixed(HLO)	0–20	80–100	0–20	0–20	0–100
12	mixed	20–80	0–20	0–20	0–20	0–100
13	mixed	20–80	0–20	0–20	20–80	0–100
14	mixed	20–80	0–20	20–80	0–20	0–100
15	mixed	20–80	0–20	20–80	20–80	0–100
16	mixed	20–80	20–80	0–20	0–20	0–100
17	mixed	20–80	20–80	0–20	20–80	0–100
18	mixed	20–80	20–80	20–80	0–20	0–100
19	mixed	20–80	20–80	20–80	20–80	0–100
20	unmixed(HLI)	80–100	0–20	0–20	0–20	0–100

GMDD
7, 7937–7987, 2014

Table 2. Mixing state after 12 h simulation.

Process	No Dynamic scenario a	Coagulation scenario b	C/E scenario c	C/E + Coag + Nucl scenario d
Mixed particle number (%)	42	79	48	51
Mixed particle mass (%)	83	85	64	76

GMDD
7, 7937–7987, 2014

Table 3. Computational times.

Process	C/E	C/E bulk	C/E hybrid	Coag	C/E + Coag	C/E + Coag bulk	C/E + Coag hybrid
Internal mixing (s)	7.1	0.11	0.4	0.06	7.3	0.14	0.5
External mixing (s)	63.2	0.3	54.2	48.4	122.8	31.5	113

GMDD
7, 7937–7987, 2014

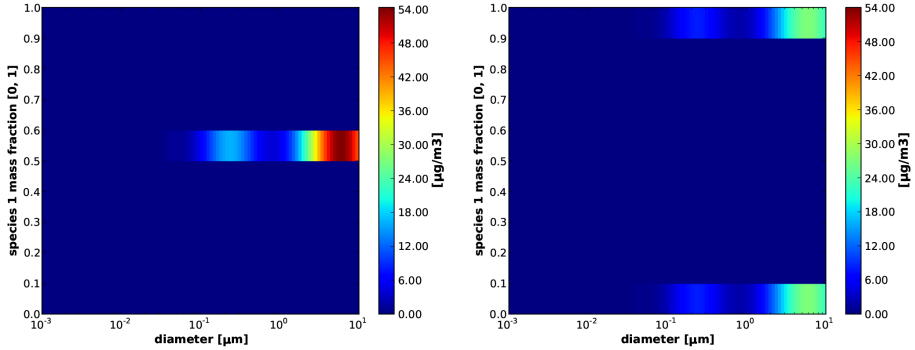

(a) Internal mixing (b) External mixing

Figure 1. Initial distribution: particle mass concentration as a function of diameter and mass fraction of species 1.

GMDD
7, 7937–7987, 2014

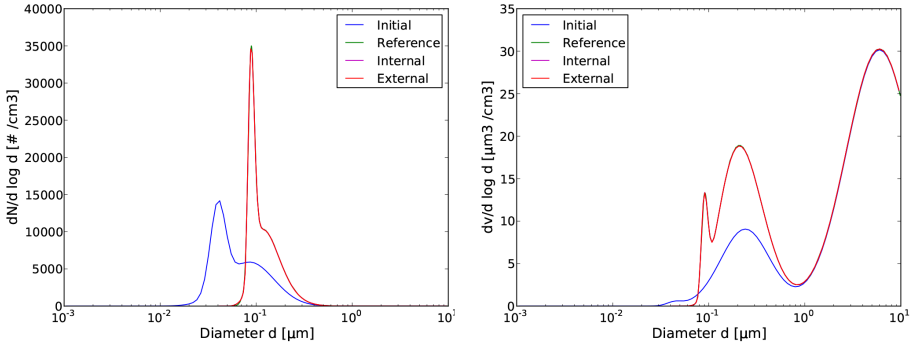

(a) Number distribution (b) Volume distribution

Figure 2. Simulation of condensation for hazy conditions: initial distribution and after 12 h.

GMDD
7, 7937–7987, 2014

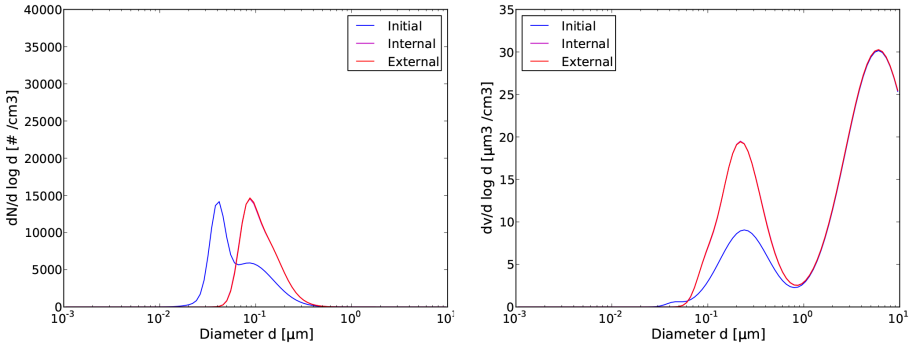

(a) Number distribution

(b) Volume distribution

Figure 3. Simulation of both coagulation and condensation for hazy conditions: initial distribution and after 12 h.

GMDD
7, 7937–7987, 2014

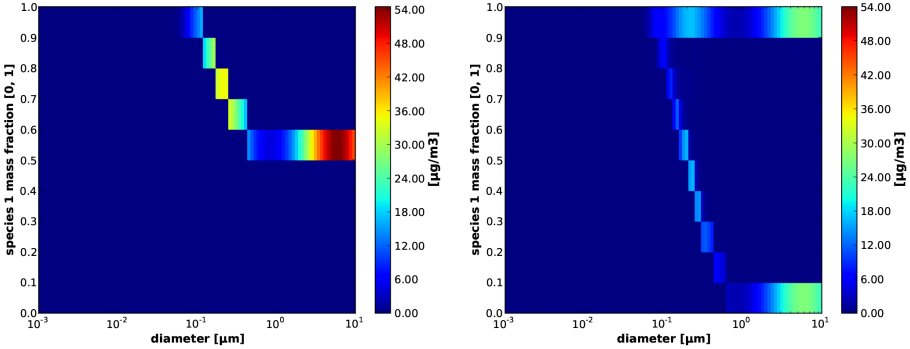

(a) Internal mixing

(b) External mixing

Figure 4. Distribution after 12 h: particle mass concentration as a function of diameter and mass fraction of species 1.

GMDD
7, 7937–7987, 2014

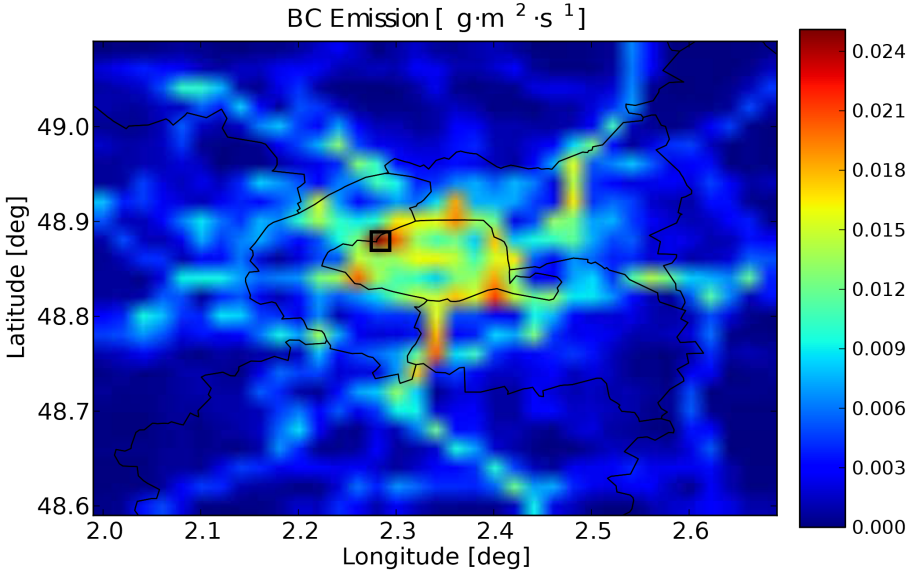

Figure 5. BC emissions over Greater Paris at 02:00 UT, 1 July 2009.

GMDD
7, 7937–7987, 2014

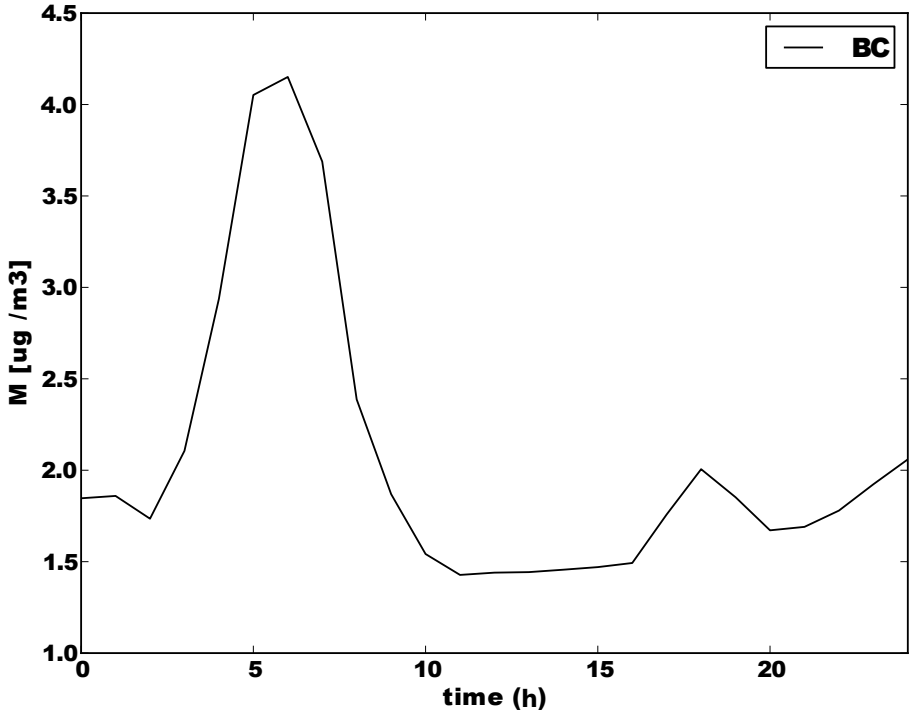

Figure 6. BC concentrations profile on 1 July 2009.

GMDD
7, 7937–7987, 2014

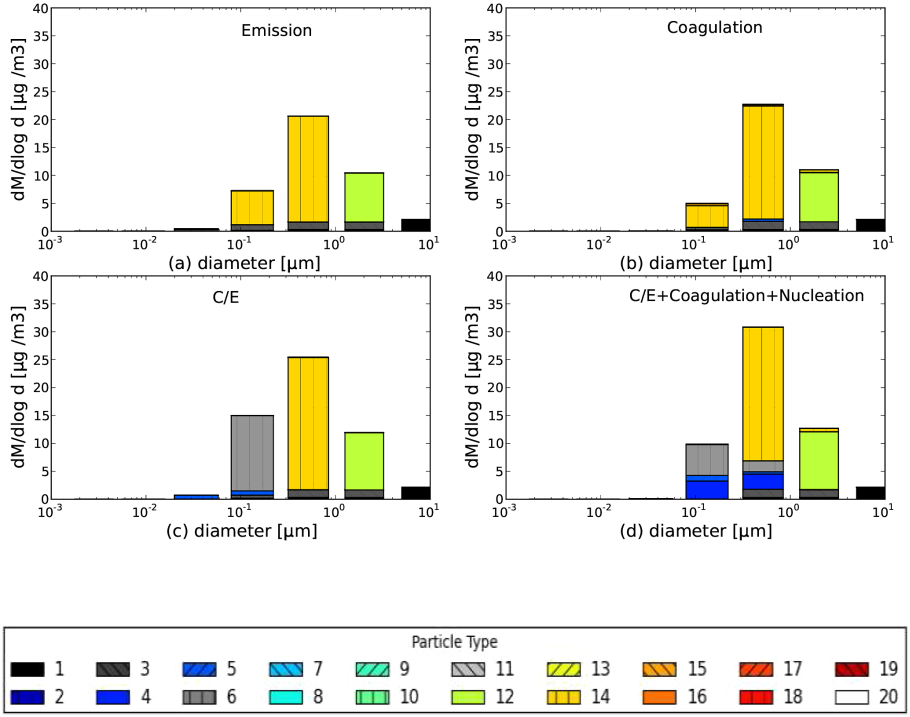

Figure 7. Mass distributions of externally-mixed particles as a function of particle diameter for the different chemical compositions.

GMDD
7, 7937–7987, 2014

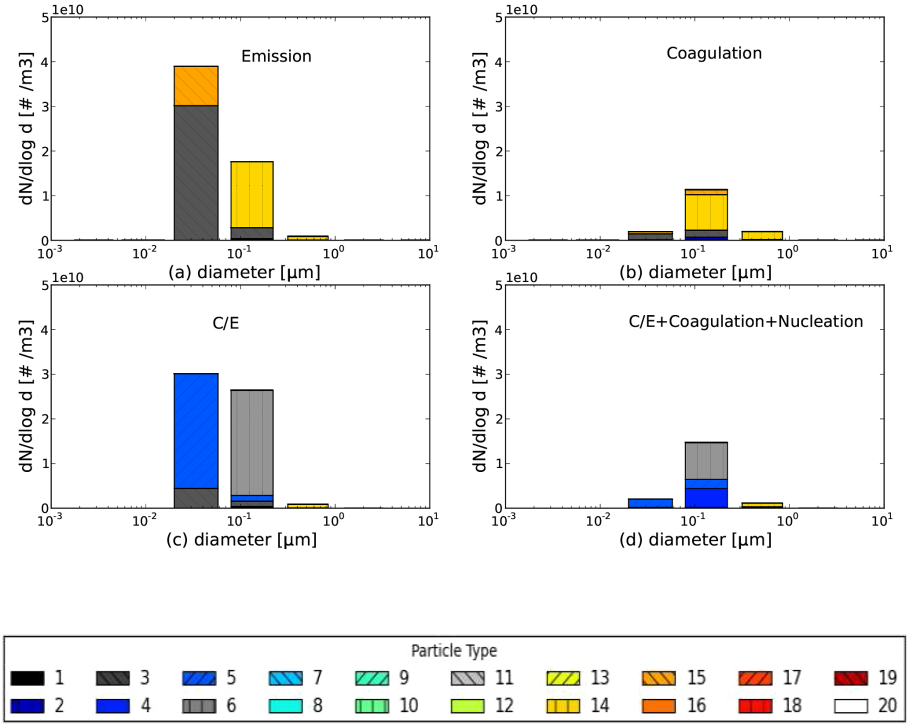

Figure 8. Number distributions of externally-mixed particles as a function of particle diameter for the different chemical compositions.

GMDD
7, 7937–7987, 2014

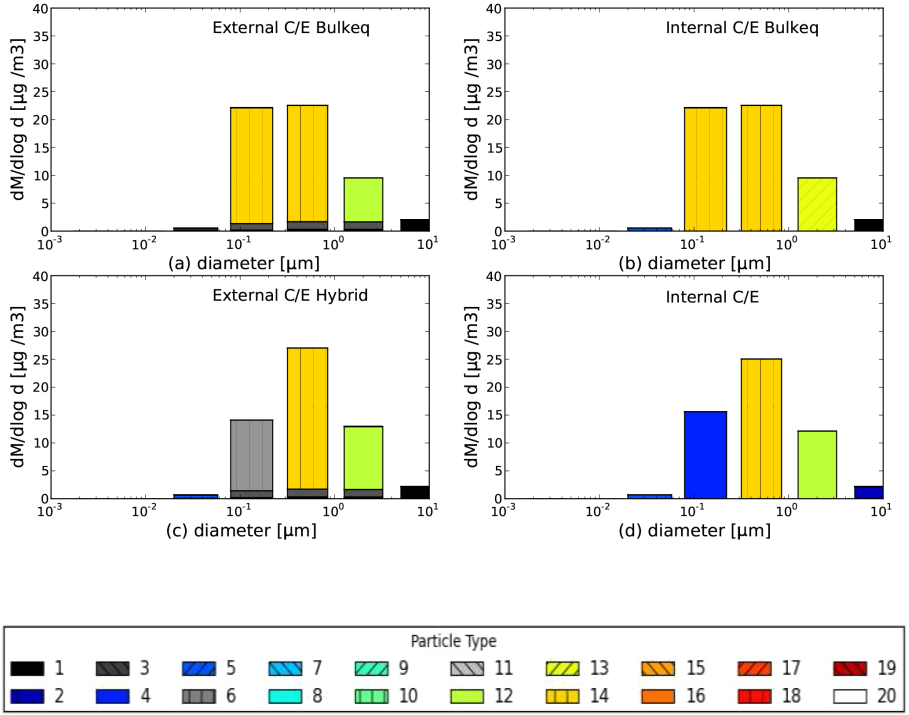

Figure 9. Composition distributions of externally-mixed and internally-mixed particles: particle mass concentration as a function of diameter for particles of different chemical compositions.

GMDD
7, 7937–7987, 2014

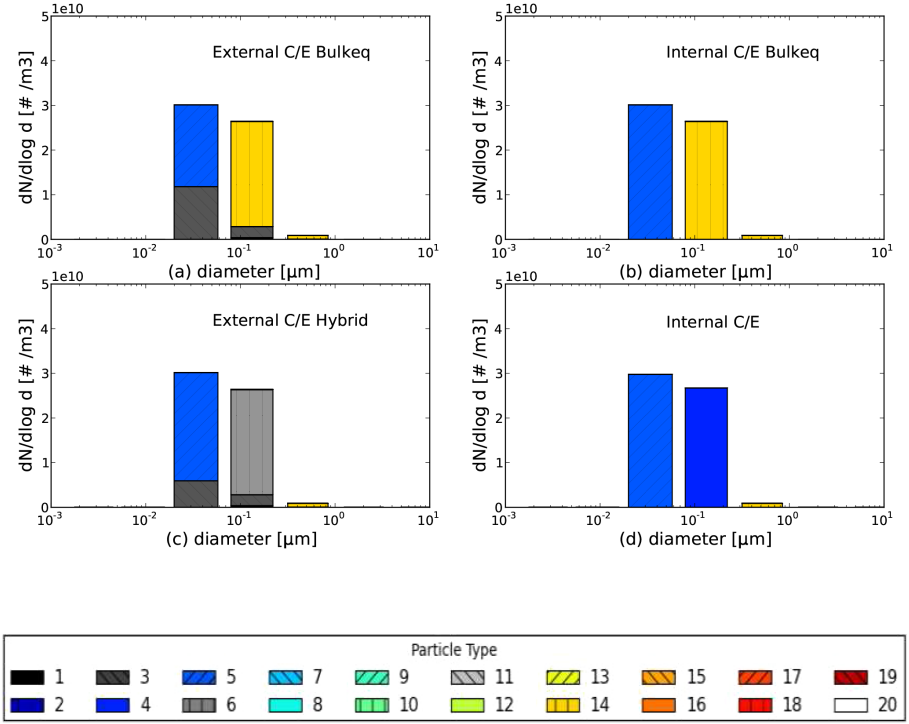

Figure 10. Composition distributions of externally-mixed and internally-mixed particles: particle number concentration as a function of diameter for particles of different chemical compositions.

GMDD
7, 7937–7987, 2014

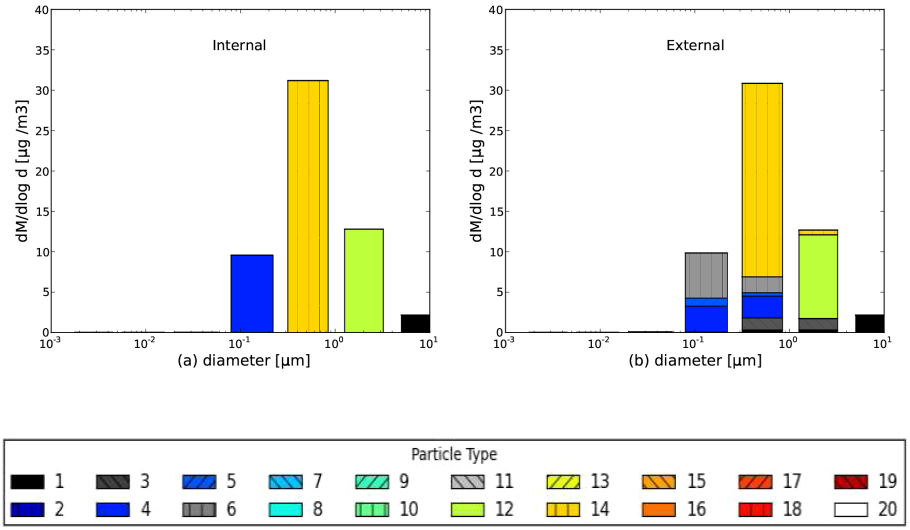

Figure 11. Mass distributions as a function of particle diameter and composition for the internal and external mixing cases.

GMDD
7, 7937–7987, 2014